AGU ADVANCING EARTH AND SPACE SCIENCES

JAMES | Journal of Advances in Modeling Earth Systems®

RESEARCH ARTICLE
10.1029/2024MS004749

On the Dependence of Simulated Convection on Domain Size in CRMs

A. M. Jenney[1], **Z. Hu**[2], **and W. M. Hannah**[3]

[1]College of Earth, Ocean, and Atmospheric Sciences, Oregon State University, Corvallis, OR, USA, [2]Department of Earth and Planetary Sciences, Harvard University, Cambridge, MA, USA, [3]Lawrence Livermore National Laboratory, Livermore, CA, USA

Key Points:

- Deep convection is suppressed in CRM domains with few grid columns due to strong subsidence warming and entrainment into small updrafts
- The suppressive effect of entrainment in domains with few grid columns can be reduced by increasing grid spacing
- Horizontal energy transport on the GCM grid modifies the effects of throttling in superparameterized simulations

Supporting Information:

Supporting Information may be found in the online version of this article.

Correspondence to:

A. M. Jenney and Z. Hu,
andrea.jenney@oregonstate.edu;
zeyuan_hu@fas.harvard.edu

Citation:

Jenney, A. M., Hu, Z., & Hannah, W. M. (2025). On the dependence of simulated convection on domain size in CRMs. *Journal of Advances in Modeling Earth Systems*, *17*, e2024MS004749. https://doi.org/10.1029/2024MS004749

Received 7 OCT 2024
Accepted 17 FEB 2025

Author Contributions:

Conceptualization: A. M. Jenney
Data curation: Z. Hu
Formal analysis: A. M. Jenney, Z. Hu, W. M. Hannah
Investigation: A. M. Jenney, Z. Hu, W. M. Hannah
Methodology: A. M. Jenney, Z. Hu
Visualization: A. M. Jenney, Z. Hu
Writing – original draft: A. M. Jenney, Z. Hu
Writing – review & editing: A. M. Jenney, Z. Hu, W. M. Hannah

Abstract We present a heuristic model to explain the suppression of deep convection in convection-resolving models (CRMs) with a small number of grid columns, such as those used in super-parameterized or multi-scale modeling framework (MMF) general circulation models (GCM) of the atmosphere. Domains with few grid columns require greater instability to sustain convection because they force a large convective fraction, driving strong compensating subsidence warming. Updraft dilution, which is stronger for reduced horizontal grid spacing, enhances this effect. Thus, suppression of deep convection in CRMs with few grid columns can be reduced by increasing grid spacing. Radiative-convective equilibrium simulations using standalone CRM simulations with the System for Atmospheric Modeling (SAM) and using GCM-coupled CRM simulations with the Energy Exascale Earth System Model (E3SM)-MMF confirm the heuristic model results.

Plain Language Summary We present a simple mathematical model that helps explain why rising cloudy air is suppressed in some computer simulations used for studying weather and climate. When the computer model has fewer columns used to represent the atmosphere, more energy is needed to sustain upward air movement because the warming of air around clouds as it sinks and compresses is stronger. We found that increasing the number of columns or making the columns wider can help reduce this effect. Computer model runs validate the results of our simple mathematical model.

1. Introduction

Convection-resolving models (CRMs) are popular tools used to simulate large-scale turbulent motions associated with clouds and convection. A multi-scale modeling framework (MMF), also known as superparameterization (SP), is a way to embed a CRM within an atmospheric general circulation model (GCM) to replace the conventional parameterizations of convection (e.g., Grabowski, 2001; Grabowski & Smolarkiewicz, 1999; Khairoutdinov et al., 2005; Randall et al., 2003). To manage their substantial computational burden, CRM domains with a limited number of grid columns are typically employed. For example, recent SP/MMF simulations have used embedded CRMs with as few as 64 columns (e.g., Hannah et al., 2020; Hannah et al., 2022; Lin et al., 2022). However, CRM domains with many more columns are sometimes used. For example, in simulations with OpenIFS (Open Integrated Forecast System) with regional SP deployment, Jansson et al. (2022) use three-dimensional CRM domains with 64 grid columns in each horizontal dimension (4096 CRM columns per GCM column), while Jansson et al. (2019) use three-dimensional CRM domains with 200 grid columns in each horizontal dimension (40,000 CRM columns per GCM column). Henceforth, we refer to the number of grid columns in a CRM domain as N.

The mass flux of a cloud updraft is balanced by clear air subsidence that causes adiabatic warming of the environment at a rate proportional to the subsidence velocity. A convective updraft can most easily maintain positive buoyancy relative to its sinking, warming environment when the updraft area is minimized, which minimizes the subsidence warming rate by spreading the subsidence mass flux over a large area (Bjerknes, 1938). In a CRM, the smallest possible updraft fraction is $1/N$ (i.e., one grid column), which increases as N decreases. Similarly, the largest possible subsidence fraction is $(N-1)/N$, which decreases as N decreases. Tompkins and Craig (1998) point out that CRM domains with too few N may generate unrealistic sporadic convection, with convection suppressed during periods of strong convective stability due to excessive subsidence warming. Furthermore, they argue that because of the nonlinear dependence of atmospheric radiation on cloud cover and relative humidity (i.e., the average heating rate of a domain oscillating between cloudy convective periods and

clear, calm periods differs from that of a domain with continuous convection), CRM domains are sufficiently large when they can support continuous ongoing convection somewhere within the domain. They arrive at a minimum of $N = 2400$ based on a scale analysis using this criterion (almost 40× greater than the 64 columns used in many modern SP/MMF simulations).

Previous work has demonstrated that MMF simulations are indeed sensitive to the N of embedded CRMs. Pritchard et al. (2014) found that decreasing N from 32 to 8 (while keeping horizontal grid spacing constant) led to an increase in the shortwave cloud forcing of an SP-GCM, primarily due to changes in low-level cloudiness. They refer to the inhibiting effects of very strong subsidence that occurs in domains with small N as convective "throttling". Pritchard et al. (2014) find that convective throttling causes the lower troposphere to remain less ventilated, resulting in increased lower tropospheric humidity, denser liquid clouds, and a cooler upper troposphere in simulations with small N.

It is well-appreciated that updraft buoyancy is reduced by dilution via entrainment of environmental air. Many previous studies show that entrainment rates are inversely related to updraft width (e.g., Hannah, 2017; Hernandez-Deckers & Sherwood, 2018; Kirshbaum & Grant, 2012; Levine, 1959; McCarthy, 1974; Morrison, 2017; Morrison et al., 2020). In a CRM domain, when N is sufficiently small, a deep convective updraft likely only occupies one grid column and hence is as wide as one grid column. In this scenario, increasing the grid spacing would thus result in a wider updraft. Consequently, it is reasonable to hypothesize that convective throttling may be reduced due to decreased updraft dilution by entrainment in the wider updraft when grid spacing is increased. In CRM simulations, updrafts reach higher maximum heights when they are wider (Khairoutdinov & Randall, 2006), and when coarser grid spacing is used (Rousseau-Rizzi et al., 2017; Tang & Kirshbaum, 2020). While the relationship between entrainment and updraft width is debated (e.g., Dawe & Austin, 2013; Xu et al., 2021), it has been shown in diverse CRM simulations that turbulent mixing decreases as grid spacing increases (Jeevanjee & Zhou, 2022; Pauluis & Garner, 2006; Tang & Kirshbaum, 2020), indicating that grid resolution impacts convective mixing.

Hence, this study focuses on understanding how convective throttling–which is an effect of N being too small to sustain ongoing convection against too-strong subsidence (Bjerknes, 1938; Tompkins & Craig, 1998)–is impacted by updraft dilution. Specifically, we explore how deep convective throttling in CRM domains with small N may be modulated by varying the horizontal grid spacing. We focus only on domains that are too small to support convective aggregation (see Muller & Held, 2012; Yanase et al., 2020).

We explore this in two sets of simulations: standalone CRM simulations in radiative convective equilibrium and SP/MMF simulations in which CRM domains are coupled to a GCM grid. The behavior in these two types of simulations is expected to differ due to their fundamental setup. In standalone CRM simulations in radiative convective equilibrium, the CRM domain must balance its own energy budget vertically. Deep convection and associated turbulent vertical fluxes are the sole mechanisms through which instability, which is continuously generated by atmospheric radiative cooling, can be removed. Thus deep convection *must* occur eventually in these simulations. In contrast, in SP/MMF simulations, embedded CRM domains can exchange energy with other CRM domains via the parent GCM grid's circulation. This coupling enables the continuous suppression of deep convection in at least a subset of the CRM domains of an SP/MMF simulation. This fundamental difference in circulation between the two simulation types is expected to lead to distinct behavior in how convective throttling manifests and how it is modulated by changes in grid spacing.

2. Heuristic Model

Here, we present a heuristic argument to explain why convective throttling occurs in CRM simulations with few grid columns in domains that are too small to support convective aggregation. We note that a similar model is presented by Bjerknes (1938) to explain the propensity for the small fractional area of deep convection.

In the absence of a net circulation, the convective and environmental mass fluxes balance,

$$w_c\sigma_c = -w_e(1-\sigma_c), \tag{1}$$

where σ_c is the fractional area of convection, w is vertical velocity, and the subscripts c and e refer to the ascending convective and descending environmental regions, respectively. In writing Equation 1, we have ignored any

horizontal variations in density, which are negligible compared to horizontal variations in vertical velocity and ascent/descent area. We note that Equation 1 holds in the embedded CRM domains of both the SP-Community Atmosphere Model (CAM) (Khairoutdinov et al., 2005, 2008) and the Energy Exascale Earth System Model (E3SM)-MMF (Hannah et al., 2020) because the domain mean vertical velocity within the embedded CRMs must be zero.

Sinking environmental air warms due to adiabatic compression at the rate $w_e(\Gamma_e - \Gamma_d)$, where $\Gamma = -\partial T/\partial z$ is the lapse rate (the rate of change of temperature, T, with height, z) and Γ_d is the dry adiabatic lapse rate. Using Equation 1 we can write subsidence warming in the descent region as

$$\frac{dT_e}{dt} = -\frac{w_c\sigma_c}{1-\sigma_c}(\Gamma_e - \Gamma_d). \tag{2}$$

The rate that temperature changes in the ascent region during undilute moist convection is

$$\frac{dT_c}{dt} = w_c(\Gamma_c - \Gamma_m), \tag{3}$$

where Γ_m is the saturated adiabatic lapse rate. To sustain a buoyancy-driven convective overturning circulation, positive buoyancy of the convective region is required. We crudely approximate this condition as

$$\frac{dT_c}{dt} > \frac{dT_e}{dt}. \tag{4}$$

In writing Equation 4 we have ignored contributions to convective region buoyancy from differences in water vapor, pressure, and condensate loading between the convective region and the environment. Additionally, we have assumed that the descending mass flux which balances the updraft mass flux, and which the updraft must be maintained against, is uniformly distributed over the environmental region. While these simplifications limit the heuristic model's quantitative accuracy, they allow us to elucidate the fundamental relationships between key variables, providing valuable insights into the underlying mechanisms driving convective throttling for small N. We can re-write Equation 4 in terms of the ascent area using Equations 2 and 3 as,

$$\sigma_c < \frac{\overline{\Gamma} - \Gamma_m}{\Gamma_d - \Gamma_m}, \tag{5}$$

where $\overline{\Gamma}$ is the domain mean lapse rate, and we have assumed negligible differences in the lapse rate between the convective and environmental region. This assumption is valid because of the relative smallness of CRM domains used in SP/MMF models and the resulting closeness of Γ_c and Γ_e, especially in the tropics due to the smallness of horizontal temperature gradients there (e.g., Romps, 2012). Equation 5 describes a (crude) limit on the maximum possible fractional convective area for a limited region with no mean circulation by the domain mean instability. The largest σ_c that can exist during ongoing convection increases with instability $\left(\overline{\Gamma}\right)$. Conversely, convective area is limited when instability is small. This is a consequence of the condition posed in Equation 4.

We thus arrive at the primary reason that CRM domains with small N throttle convection. N limits the minimum value that σ_c can assume: The smallest possible value of σ_c in a CRM domain is $1/N$. This number decreases as N increases. The threshold instability (Γ^*) needed to maintain a convectively driven overturning circulation in at least one grid column during undilute convection in a CRM can be inferred from Equation 5:

$$\Gamma^* = \frac{1}{N}(\Gamma_d - \Gamma_m) + \Gamma_m. \tag{6}$$

The right hand side of Equation 6 is a weighted average of the dry and moist adiabatic lapse rates, which decreases and approaches the moist adiabatic lapse rate as N is increased. The dashed lines in Figure 1 show Γ^* computed from Equation 6 for N ranging from 2 to 512 columns. Differences in Γ^* between N are large for very small N, and converge toward Γ_m as N increases.

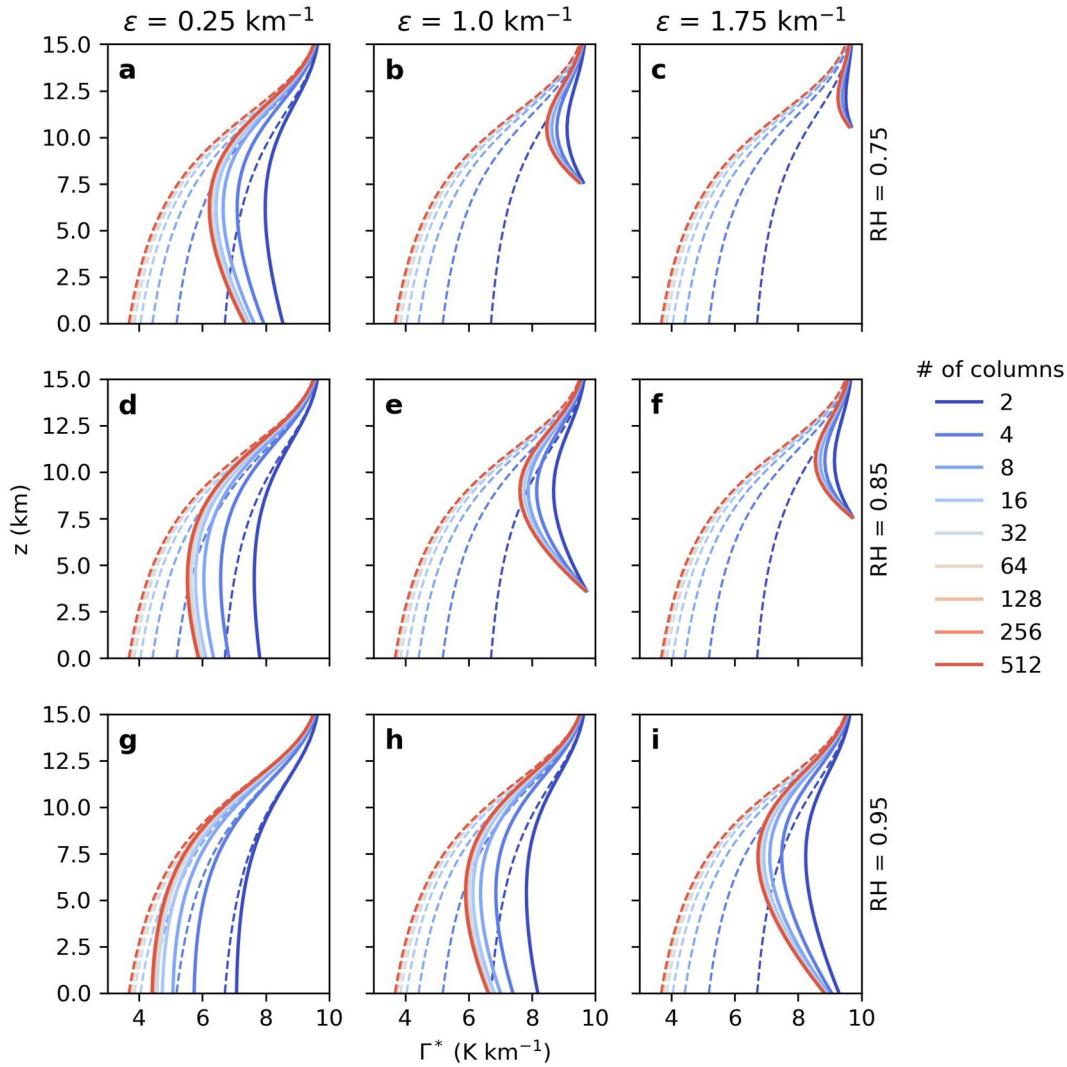

Figure 1. The critical lapse rate, Γ^*, needed to maintain convection (i.e., to satisfy Equation 4) for undilute (dashed lines; see Equation 6) and diluted (solid lines; see Equation 9) convection, for domains ranging from 2 to 512 columns, given a range of entrainment rates (increasing by column left to right) and relative humidities of entrained air (increasing by row, top to bottom).

Equation 6 and the dashed lines in Figure 1 show that domains with small N require more instability to maintain undilute convection. However, in CRM simulations and in reality, buoyant convection does not occur without entrainment, which can substantially dilute updraft buoyancy. We modify Equation 3 for entraining convection as

$$\frac{dT_c}{dt} = w_c(\Gamma_c - \Gamma_m - \epsilon\beta) \tag{7}$$

where ϵ is the fractional entrainment rate (with units of inverse length) and β is a dilution factor that depends on the difference in temperature and humidity between the updraft air and the entrained air, which we will crudely approximate as

$$\beta = T_c - T_{\text{entrained}} + \frac{L_v}{c_p}(q_s - q_{\text{entrained}}). \tag{8}$$

In Equation 8, L_v is the latent heat of vaporization, c_p is the specific heat capacity of dry air, q is the water vapor mixing ratio, and the subscript "entrained" indicates quantities associated with the entrained air. In writing (Equation 8), we have assumed that the convective region is saturated (q_s) and have neglected differences in latent heating due to ice processes. Using Equation 7, we can rewrite the threshold instability needed to maintain a convectively driven overturning circulation for entraining convection as

$$\Gamma^* = \frac{1}{N}(\Gamma_d - \Gamma_m) + \Gamma_m + \epsilon\beta\left(1 - \frac{1}{N}\right). \tag{9}$$

Entrainment of unsaturated air increases Γ^*. This is seen with the solid lines in Figure 1, which show the variation in Γ^* calculated using Equation 9 that results from varying ϵ between 0.25 and 1.75 km^{-1} and the relative humidity of the entrained air between 75% and 95%. We omit plotting $\Gamma^* > \Gamma_d$. When entrained air is relatively dry, even modest entrainment rates contribute to a large amplification of Γ^* because of strong dilution. Similarly, we see a strong increase in Γ^* for the converse: when entrained air is humid (95% relative humidity) but the entrainment rate is strong. The key point here is that entrainment dilution has a strong impact on Γ^*.

Comparison of Equation 9 with Equation 6 reveals that the decrease in Γ^* with increasing N is associated with undilute processes. For a constant value of entrainment dilution, $\epsilon\beta$, entrainment actually reduces differences in Γ^* between N. This can be seen by comparing the spread between the dashed lines and solid lines in each panel of Figure 1, which is smaller for the entraining case (solid lines) than the undilute case (dashed lines). However, as we mentioned in Section 1, N may directly affect ϵ via a control on updraft width by limiting the number of columns available for convection. Convection-resolving model domains with small N may thus amplify $\epsilon\beta$ by forcing updrafts to occupy only one grid column, and hence be physically small and entrain more than they would if they could occupy multiple columns and be wider. As a result, convective throttling due to small N may be enhanced by entrainment dilution, and may be reduced by coarsening the grid spacing to reduce mixing. We will explore this question next using both standalone CRM and GCM-coupled SP/MMF simulations.

3. Methods

3.1. Simulations

3.1.1. Standalone CRM Simulations: SAM

We use the System for Atmosphere Modeling (SAM; Khairoutdinov & Randall, 2003), version 6.10.6, configured as a cloud-resolving model with doubly periodic lateral boundaries. We run 3-D simulations with 8 ($N = 64$), 16 ($N = 256$), 32 ($N = 1,024$), 64 ($N = 4,096$), 128 ($N = 16,384$), and 256 ($N = 65,536$) grid columns in each horizontal direction, and with horizontal grid spacings of 62.5, and 250 m, 1 , and 4 km. We use 60 vertical levels with a model top located near 26 km and a rigid-lid top boundary condition. Between the surface and 2.5 km, the vertical grid spacing linearly increases from 75 to 500 m, and is held constant at 500 m above 2.5 km. A sponge layer is located above 18 km. Sea surface temperature (SST) is fixed uniformly at 303K.

Simulations are non-rotating and forced with the same prescribed radiative heating profile, which was obtained from an equilibrated SAM simulation run in radiative-convective equilibrium with interactive radiation (Rapid and Accurate Radiative Transfer Model for General Circulation Models, Iacono et al., 2008). We use prescribed, rather than interactive radiation, to inhibit the influence of cloud and water vapor radiative feedbacks on the results (i.e., to more cleanly isolate the influence of N and grid spacing on the results). We include the radiative heating forcing profile in the supplemental material (Figure S3 in Supporting Information S1).

We use a single moment microphysics scheme (Khairoutdinov & Randall, 2003) which uses an instantaneous saturation adjustment to determine the partitioning between water vapor and cloud condensate, the latter of which is divided into liquid and/or ice phases based on temperature. Similarly, precipitating water is diagnostically partitioned into rain, snow, and graupel based on the temperature. The saturation adjustment occurs at each effective time step.

Each run is initialized from the same warm, humid temperature and moisture profile (Figure S1 in Supporting Information S1) with white noise temperature perturbations on the order of 0.01 K applied to the lowest 5 model layers to initiate convection. A simple Smagorinsky-type scheme (Khairoutdinov & Randall, 2003) computes

sub-grid scale momentum and scalar tendencies. Domain-averaged horizontal wind is nudged to zero at each vertical level with a nudging time scale of 1 hr. Each simulation includes a 100-day spin-up phase. Unless otherwise noted, a 20-day period after spin-up is used to compute equilibrium statistics (see Figure S2 in Supporting Information S1 for time series over the entire 120-day simulation period). Domain-mean statistics are sampled every 2 min and then averaged to estimate hourly domain-mean statistics.

For completeness, we also ran two-dimensional simulations with $N = 16$ and $N = 128$ and 1 km grid spacing. The sensitivity of convective statistics and domain mean quantities to N in these two-dimensional simulations was similar to that observed in the three-dimensional runs, thus we omit those results. Other studies have investigated the sensitivity of convection to CRM dimensionality (Hsu et al., 2024; Liu et al., 2023), which is not a goal of our study.

3.1.2. Global MMF Simulations: E3SM-MMF

The Energy Exascale Earth System Model (E3SM) was originally forked from the NCAR Community Earth System Model (CESM), but all model components have undergone significant development since Golaz et al. (2019). The dynamical core uses a spectral element method on a cubed-sphere geometry, while physics calculations are performed on a finite volume grid that is slightly coarser than the dynamics grid, but more closely matches the effective resolution of the dynamics (Hannah et al., 2021).

The multi-scale modelling framework (MMF) configuration of E3SM (E3SM-MMF) was originally adapted from SP-CAM and reproduces the general behavior of its predecessor (Hannah et al., 2020). The embedded CRM is adapted from SAM, but rewritten in C++ using the performance portability library of Yet Another Kernel Launcher (YAKL, Norman et al., 2023) to facilitate GPU acceleration. Microphysical processes are parameterized with a single moment scheme, and sub-grid scale turbulent fluxes within the CRM are parameterized using a diagnostic Smagorinsky-type closure. There is an additional boundary layer scheme outside of the CRM based on Holtslag and Boville (1993). This allows surface momentum fluxes to be mixed through the boundary layer prior to the global dynamics, which reduces biases in near-surface wind.

E3SM-MMF uses a 60 layer vertical grid with 50 levels in the embedded CRM. The embedded CRM in E3SM-MMF uses a two-dimensional domain with 64 CRM columns in a north-south orientation and 2 km horizontal grid spacing. The global physics time step is set at 20 min with a CRM time step of 10 s. The CRM variance transport scheme of Hannah and Pressel (2022) is enabled to reduce grid-scale noise caused by variance trapping in the CRM (Hannah et al., 2022).

E3SM-MMF was configured for radiative-convective equilibrium (RCE) according to the RCE model intercomparison project (RCEMIP) protocol (Wing et al., 2018). This includes globally homogeneous surface temperature of 300K and globally homogeneous downward shortwave radiation. The initial condition was created from a 100-day run starting from an analytic initial condition. The standard global cube-sphere grid was used with 30×30 spectral elements per cube face and 2×2 finite volume physics cells per element (i.e., ne30pg2), with an approximate physics grid spacing of 150 km. Each simulation was run for 198 days using 64 Perlmutter GPU nodes at the National Energy Research Scientific Computing Center (NERSC).

3.2. Methods for Diagnosing Entrainment and Detrainment Rate

We will present some results relating to diagnosed fractional entrainment and detrainment rate. Here we document how they are calculated. We first estimate the entrainment and detrainment rate through a simple entraining-detraining bulk-plume model (e.g., De Rooy et al., 2013; Yano, 2014):

$$\frac{\partial \phi_u}{\partial z} = -\epsilon\left(\phi_u - \phi_n\right) + S_u \tag{10}$$

$$\frac{1}{M}\frac{\partial M}{\partial z} = \epsilon - \delta \tag{11}$$

where ϕ is a relatively conserved variable, subscripts "u" and "n" denote averages across convective updraft grid cells and non-updraft grid cells, S_u is the net source of ϕ within updraft, ϵ and δ represent the fractional entrainment rate and detrainment rates, M represents the convective updraft mass flux, and z is height. Here, we

choose ϕ as the total non-precipitating water (i.e., water vapor plus liquid and ice cloud mixing ratio). S_u is evaporation of precipitation minus cloud-to-precipitation conversion averaged across updraft grid cells. Convective updraft grid cells are those with cloud mixing ratios greater than 10^{-5} kg kg^{-1} and upward vertical velocities greater than 1 m s^{-1}. Non-updraft grid cells are defined as those with cloud water mixing ratios smaller than 10^{-5} kg kg^{-1}. Horizontally averaged ϕ_u, ϕ_n, S_u, and M were saved as part of our domain-mean statistics outputs.

In addition to the above single plume model, we also used a spectrum plume method to diagnose the entrainment rate distribution (Kuang & Bretherton, 2006). Unlike the single plume model which assumes all the updrafts have the same entrainment rate profile, the spectrum plume model allows updrafts to have a spectrum of entrainment rates. Here we briefly describe the procedure of calculating entrainment rate distribution used in Kuang and Bretherton (2006). First we need to calculate the convective updraft mass flux distribution in the space of frozen moist static energy (FMSE) and height. Frozen moist static energy is defined as $c_pT + gz + L_vq - L_fq_i$, where T is temperature, g is gravitational acceleration, L_f is the latent heat of fusion, respectively, and q, q_i are the mixing ratios of water vapor and ice, respectively. Then we specify a set of fractional entrainment rate values, and calculate the FMSE profile of an entraining plume using the mean FMSE in the updraft at the cloud base for each fractional entrainment rate. Then, at each level, we count how many mass fluxes fall into each entrainment rate interval according to their FMSE. Essentially we get mass flux distribution in the space of entrainment rate and height. To ensure sufficient 3-D output for calculations related to this spectrum plume method, we extended the 1 km-resolution simulations with instantaneous 3-D fields saved every 30 min as follows: $N = 16 \times 16$ for 320 days, $N = 32 \times 32$ for 160 days, $N = 64 \times 64$ for 160 days, $N = 128 \times 128$ for 80 days, and $N = 256 \times 256$ for 20 days.

4. Simulation Results

4.1. Standalone CRM (SAM)

N has a clear impact on the behavior of limited-domain CRM simulations. Figure 2 shows time series of convective available potential energy (CAPE), precipitation, environmental vertical velocity w_e (defined as the mean vertical velocity at 4 km for grid cells with cloud condensate less than 10^{-5} kg kg^{-1}), and the free troposphere lapse rate (calculated between heights of 1 and 12 km). As hypothesized by Tompkins and Craig (1998), the temporal variability of precipitation, instability, and vertical velocity is generally larger for small N. This is a consequence of excessive subsidence warming with small N, which stabilizes the domain, with periods of quiescence between convective events as radiative cooling and surface fluxes regenerate instability. In comparison, domain mean precipitation and w_e are continuous for large N. Tompkins and Craig (1998) estimate that a domain with about $N = 2400$ (approximately 50×50 columns in each horizontal direction) is needed to simulate continuous convection. Qualitatively, for our simulations, there is a large reduction in the temporal variance of domain mean precipitation and w_e between 32×32 and 64×64, consistent with Tompkins and Craig (1998).

An exception to the previous discussion occurs for the simulations with the finest grid spacing of 62.5 m. Continuous convection is not achieved at this grid spacing, even for the largest N (Figure 2e). The temporal variance in CAPE increases with N, instead of decreasing as it does for the other grid spacings. We note that both the aspect ratio of grid cells (horizontal to vertical = 0.125) and the physical domain size (16×16 km for $N = 256 \times 256$) are unusually small for deep convective simulations, and so we choose not to explore this behavior further.

In addition to becoming more variable, domain mean CAPE also increases as N decreases. This is true even at the grid spacing of 62.5 m. This is a consequence of convective throttling: For small domains, more instability is needed to maintain a convective overturning circulation (Equation 6). The suppression of convection in domains with small N causes the accumulation of instability, which is otherwise efficiently removed by convection in domains with large N (Tompkins & Craig, 1998). However, we see a decrease in domain mean CAPE for each increase in N. In other words, we do not see a convergence as the N approaches the Tompkins and Craig (1998) limit of 2,400. The changes in CAPE are also evident in the free-troposphere lapse rate (last row in Figure 2), which increases as N decreases. This dependence of the lapse rate on N, which is larger for small N, is consistent with predictions from the heuristic model (Figure 1).

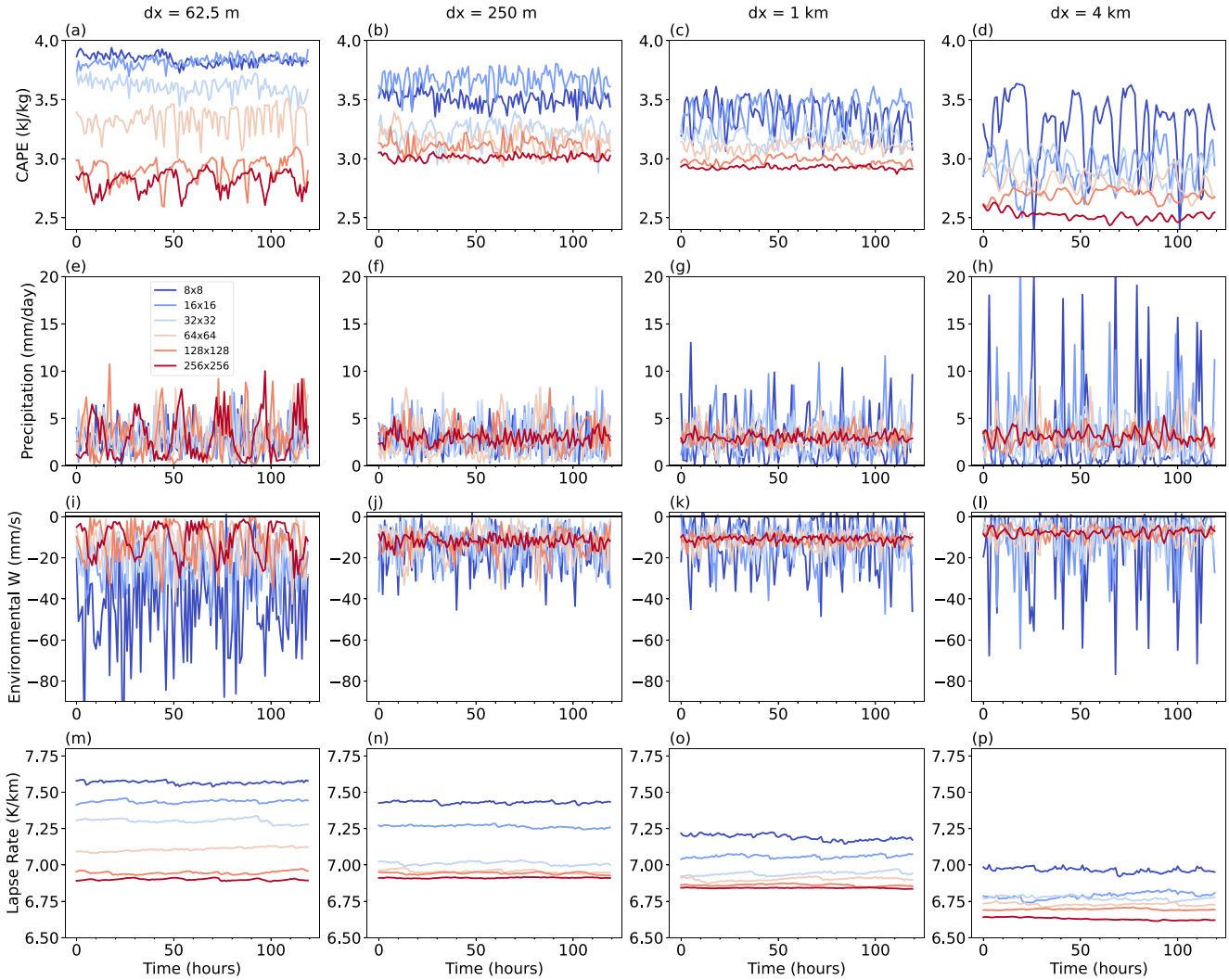

Figure 2. For days 101–105 in SAM simulations, time series of (first row) convective available potential energy (CAPE) (second row) surface precipitation (third row) environmental vertical velocity, and lapse rate (last row) for horizontal grid spacings of (left column) 62.5 m (center left column) 250 m (center right column) 1 km, and (right column) 4 km. Environmental vertical velocity is evaluated at 4 km and is calculated by averaging the vertical velocity across all grid cells with cloud mixing ratio less than 10^{-5} kg kg^{-1}. Lapse rate is calculated based on the temperature difference between model levels at $z = 12$ km and $z = 1$ km.

Figure 3 shows profiles of domain averaged mean state quantities from the SAM simulations as a function of N (line colors) and grid spacing (columns). The first row of Figure 3 shows that the convective mass flux increases as N decreases. The simulations in this study are in radiative-convective equilibrium with identical prescribed radiative cooling rates. This means that, ignoring the minor contribution from vertical turbulent fluxes, the heating due to convection (the net condensation minus evaporation rate) must also be identical across the simulations. The convective mass flux and gross condensation rate are intimately related (Kogan, 2021, 2022). Thus, there must be more evaporation occurring in the simulations with small N (see Figure S3 in Supporting Information S1), which have larger convective mass fluxes, in order to produce equivalent convective heating rates as simulations with large N. This suggests that for larger N, convection is more efficient at heating the free troposphere, as less of the condensation is offset by evaporation. The second row of Figure 3 shows that relative humidity increases as N decreases, consistent with there being more condensate evaporation and mixing between the updraft and environment for small N.

High cloud fractions are also larger in small domains (Figure 3b). This is likely due to two factors: first, the larger convective mass flux below the anvil level, which enhances the detrainment of cloud material at the anvil level; and second, the higher relative humidity, which slows anvil cloud evaporation. These processes contribute to the

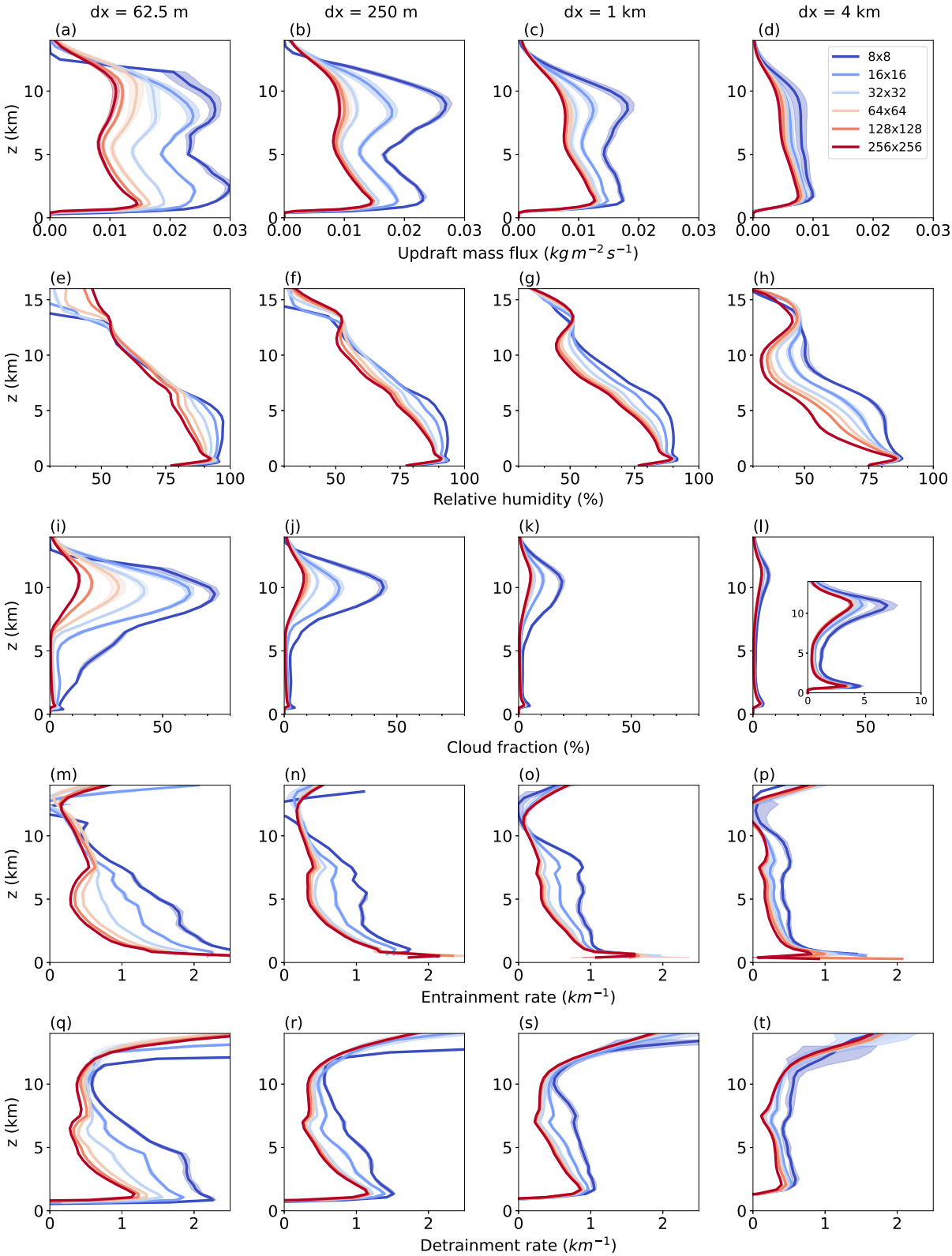

Figure 3.

first order balance between cloud formation and dissipation that determines overall anvil cloud fraction (Beydoun et al., 2021; Seeley et al., 2019).

Next we discuss the increased evaporation in domains with smaller N. The critical instability in Equation 6 is the threshold lapse rate for *one grid column* to buoyantly convect without violating condition (Equation 4). For a given value of $\Gamma > \Gamma^*$, the number of grid columns available for convection increases with N. This implies, for a fixed grid spacing, that increasing N also allows updrafts to be *physically* wider by occupying more grid cells. Figure 4a shows that we indeed see a widening of the updraft width distribution as N is increased, with a reduction in the number of small updrafts and an increase in the number of wider updrafts. Convective entrainment rates may be larger for physically small updrafts (e.g., Hernandez-Deckers & Sherwood, 2018; Khairoutdinov & Randall, 2006; Kirshbaum & Grant, 2012; Levine, 1959; McCarthy, 1974; Morrison, 2017; Morrison et al., 2020). Thus, enhanced updraft dilution due to enhanced entrainment into smaller updrafts may be causing increased evaporation in domains with smaller N. Figure 4b shows that the distribution of entrainment rates diagnosed using the spectral plume method (see Section 3.2) indeed shifts toward smaller values as N is increased and updrafts become wider.

From this argument, it logically follows that the impact of N on convective throttling should be reduced by increasing the grid spacing to make updrafts *physically* wider such that dilution by entrainment is also reduced. The profiles shown in Figure 3 consistently support this expectation. As the grid spacing is coarsened, the spread in the bulk fractional entrainment rate with N decreases *and* the distribution of bulk entrainment rates shifts toward smaller magnitudes. Furthermore, the spread in the convective mass flux and cloud fraction with N reduces as grid spacing is coarsened, suggesting that convective throttling is also reduced. Finally, the troposphere lapse rate and its spread with N is reduced as grid spacing is coarsened (Figures 2m–2p), which is consistent with the heuristic model results shown in Figure 1. Jeevanjee and Zhou (2022) also show that the updraft mass flux, relative humidity, and anvil cloud fraction increase for finer horizontal grid spacing as a result of increased mixing.

The final row of Figure 3 shows how bulk detrainment varies with N. The termination of updrafts contributes to bulk detrainment, and occurs when updrafts reach their level of neutral buoyancy, can no longer ascend, and thus transfer their remaining mass to the environment. We refer to this type of detrainment as dynamical detrainment (see De Rooy et al., 2013). From Section 2, it can be intuited that dynamical detrainment should be larger for smaller N. For small N, compensating subsidence warming is strong because σ_c is forced to be large. As a result, an existing updraft is more likely to become neutrally buoyant at a lower altitude than in a domain with large N (and with a smaller σ_c, assuming all else equal). Note that this is an undilute effect. However, the sensitivity of dynamical detrainment to N is likely exacerbated by updraft dilution by entrainment. That is, updrafts in domains with smaller N are *even more* likely to reach their levels of neutral buoyancy at lower altitudes because of enhanced dilution. Finally, the enhancement of turbulent mixing between the updraft and the environment for small N likely also contributes to the increased turbulent (in addition to dynamical) detrainment for small N. This is supported by the increase in detrainment rate for smaller N, and the reduction in the differences between detrainment rates with N for coarser grid spacings.

Profiles from SAM simulations with the same setup but with interactive radiation are shown in Figure S4 in Supporting Information S1. In general, interactive radiation does not change the sensitivity of domain mean quantities to N. We note some exceptions: in the upper troposphere, differences in relative humidity between N are slightly enhanced in simulations with interactive radiation; while differences in the convective mass flux are slightly reduced.

In summary, CRM domains with small N throttle convection by producing too-strong subsidence. Additionally, we show that CRM domains with small N *also* limit updraft width and increase convective entrainment rates.

Figure 3. Sensitivity of domain mean profiles to computational domain size across horizontal resolutions of 62.5 km (left column), 250 m (center left column), 1 km (center right column), and 4 km (right column). The rows from top-to-bottom are (a–d) relative humidity (e–h) updraft mass flux (i–l) cloud fraction (m–p) fractional entrainment rate, and (q–t) fractional detrainment rate. Entrainment and detrainment are diagnosed using the bulk plume model described in Section 3.2. Shaded uncertainty range is estimated by dividing each 20-day simulation into 8 non-overlapping 2.5-day time block and calculating the standard deviation across the 8 time blocks. In panel i, the inset plot zooms in on a smaller range of cloud fraction to provide greater clarity.

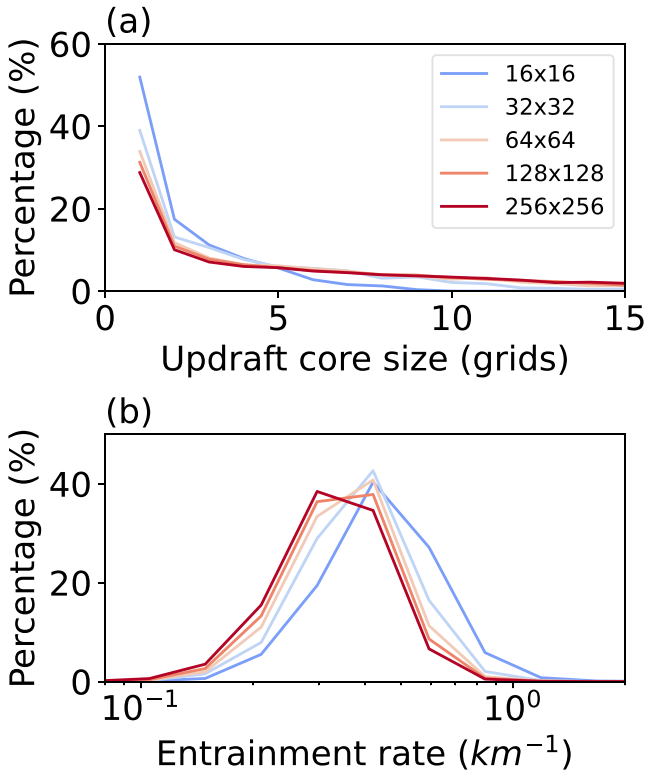

Figure 4. Probability distributions of (a) updraft core size and (b) entrainment rate at an altitude of 6 km for simulations with 1 km grid spacing. Updraft cores are defined as contiguous grid cells with an upward velocity exceeding 1 m s^{-1} and a cloud mixing ratio exceeding 10^{-5} kg kg^{-1}. Updraft core size is defined as the number of grid cells in each updraft core. The mass flux of each updraft core is used as the weight to calculate the probability distribution of core sizes. The entrainment rate distribution is diagnosed using the spectrum plume model described in Section 3.2.

Thus, convective throttling in standalone CRM simulations can be reduced either by increasing N or by increasing the grid spacing to reduce mixing.

4.2. GCM-Coupled (E3SM-MMF)

We now assess sensitivity to the N of embedded CRMs in SP/MMF simulations. The CRMs in these simulations are different from those analyzed in Section 4.1 in two primary ways. First, they have interactive radiation, and thus cloud and water vapor radiative feedbacks will affect their statistics. Second, the individual CRMs are not in radiative-convective equilibrium because they are able to laterally exchange energy with other CRM domains via the parent GCM grid's circulation. This second point is important because this coupling enables low-instability (i.e., "throttled") CRMs to effectively "export" their instability to higher instability CRMs via the GCM circulation, enabling continuous convective suppression in at least a subset of the CRM domains, unless processes outside of the CRM, such as GCM advection and fluxes from the surface component models, conspire to create adequate instability to encourage convection. In contrast, in the standalone CRM simulations turbulent vertical fluxes, including deep convection, are the sole mechanism through which continuous radiative cooling is balanced.

Figure 5 shows time series of various quantities from the E3SM simulations. Figure 6 shows domain mean (i.e., across all GCM grid cells) profiles, averaged from days 110–200. Precipitable water is larger for smaller N, with a roughly 5 mm spread between $N = 32$ and $N = 256$, consistent with the relative humidity being larger for smaller N, which we also found in the standalone simulations. However, GCM coupling greatly reduces the spread in relative humidity with N that we observe in the standalone simulations, with some levels even having negligible or no differences in relative humidity in E3SM-MMF. The increase in precipitable water for smaller N is driven primarily by larger relative humidities at low levels, as in Pritchard et al. (2014). This is consistent with an increase in low cloud fraction (6i, 6j) and shortwave cloud radiative effect (Figure 7) for smaller N, which was also found in Pritchard et al. (2014).

As in Pritchard et al. (2014), we find that the convective mass flux *decreases* for smaller N in the SP/MMF configuration (Figures 6c and 6d). Note that this is the opposite result to the one we found for standalone CRM simulations (Figures 3e–3h), in which the convective mass flux *increases* for smaller N. The convective mass flux used to construct these profiles is saved as a diagnostic calculated online using cloudy grid cells exceeding a 2 m s^{-1} threshold vertical velocity (which is the same threshold used in the convective mass flux diagnostic from SP-CAM). Figure S5 in Supporting Information S1, constructed from 32-day extensions of the 1 km simulations, shows that the convective mass flux computed using this 2 m s^{-1} threshold is smaller by an order of magnitude, has a different shape, and a re-ordered variation with N from one computed with a lower threshold of 0.1 m s^{-1}. Thus, the profiles shown in Figures 6e and 6f should be considered as the convective mass flux of only the fastest updrafts, rather than the total convective updraft mass flux, as the high 2 m s^{-1} threshold is likely causing many updrafts, especially for small N, to be missed.

Profiles of the large-scale mass flux (the intensity of the GCM-grid overturning circulation) in Figures 6k and 6l show that the intensity of the large-scale (i.e., GCM grid scale) overturning circulation is larger for small N. This, combined with the relative invariance of the dry static stability (Figures 6g and 6h) with N suggests that, as we expect, there is indeed more energy being circulated via the GCM grid scale circulation for smaller N. This is because CRMs with small N have a harder time taking care of their own instability via deep convection (i.e., they are throttled) so they "export" it to neighboring GCM grid cells via the large-scale (i.e., GCM) circulation. Figures 5e–5h shows that the ascent area and (for 1 km grid spacing) the spatial variance of vertically integrated moist static energy $\left(\overline{\langle h \rangle'^2}\right)$ is increased for smaller N, consistent with convection being more organized or

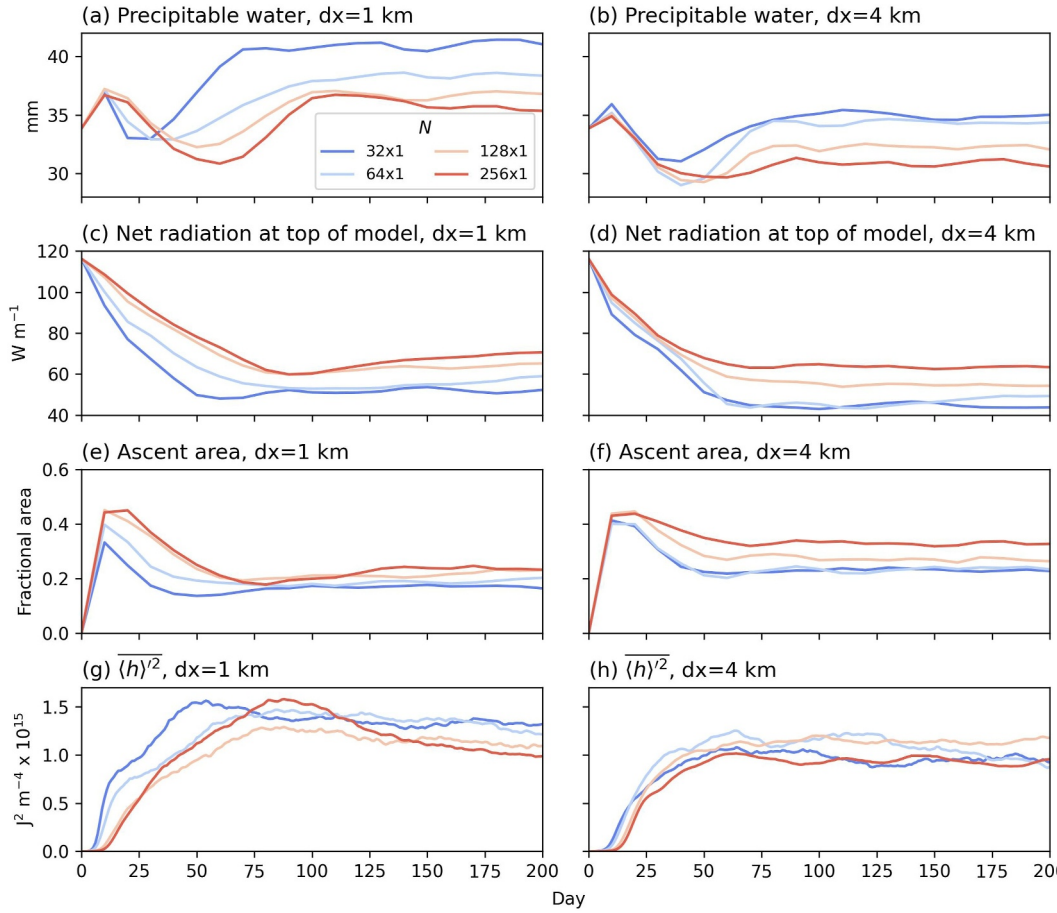

Figure 5. Time series of (a), (b) precipitable water (c), (d) the net radiative flux at the top of the model (e), (f) ascent area, and (g), (h) the spatial variance of vertically integrated moist static energy, $\overline{\langle h \rangle'^2}$, for E3SM-MMF simulations. Left (right) column is for simulations with embedded CRM horizontal grid spacing of 1 km (4 km).

clustered. This is likely a consequence of convective throttling for smaller N, which concentrates convection into a smaller, moister, and more unstable region. Interestingly, the decrease in both organization and precipitable water with N is incongruous with how these two fields typically vary together in simulations (i.e., convective organization tends to dry out the domain) (reviewed in Wing et al., 2017).

Differences between simulation fields with N as grid spacing is increased from 1 to 4 km are more subtle for the GCM-coupled CRM simulations here than they are in the standalone CRM simulations shown in Section 4.1. Precipitable water for all N decreases by about 5 mm, with a small reduction in spread with N, consistent with a decrease in mixing as CRM grid spacing is coarsened, as in the standalone CRM simulations (also Pauluis & Garner, 2006; Tang & Kirshbaum, 2020; Jeevanjee & Zhou, 2022). This may be driven, in part, by a reduction in mid-tropospheric relative humidity and associated cloudiness, which in-turn leads to a slight reduction in the magnitudes of the shortwave and net cloud radiative effects at 4 km grid spacing. However, interactive radiation also makes the coarser simulation colder by about 2–5 K (not shown), which could also be driving the reduced precipitable water at 4 km. The increased ascent area and decreased $\overline{\langle h \rangle'^2}$ shows that large-scale convective organization is also slightly decreased for 4 km grid spacing, compared to 1 km grid spacing as throttling is reduced. Differences between N are comparable between grid spacing, except for the profiles of updraft mass flux, cloud fraction, and large-scale mass flux between about 800 and 400 hPa. Thus, for GCM-coupled simulations, throttling appears to only be reduced in the mid-troposphere as grid spacing is coarsened.

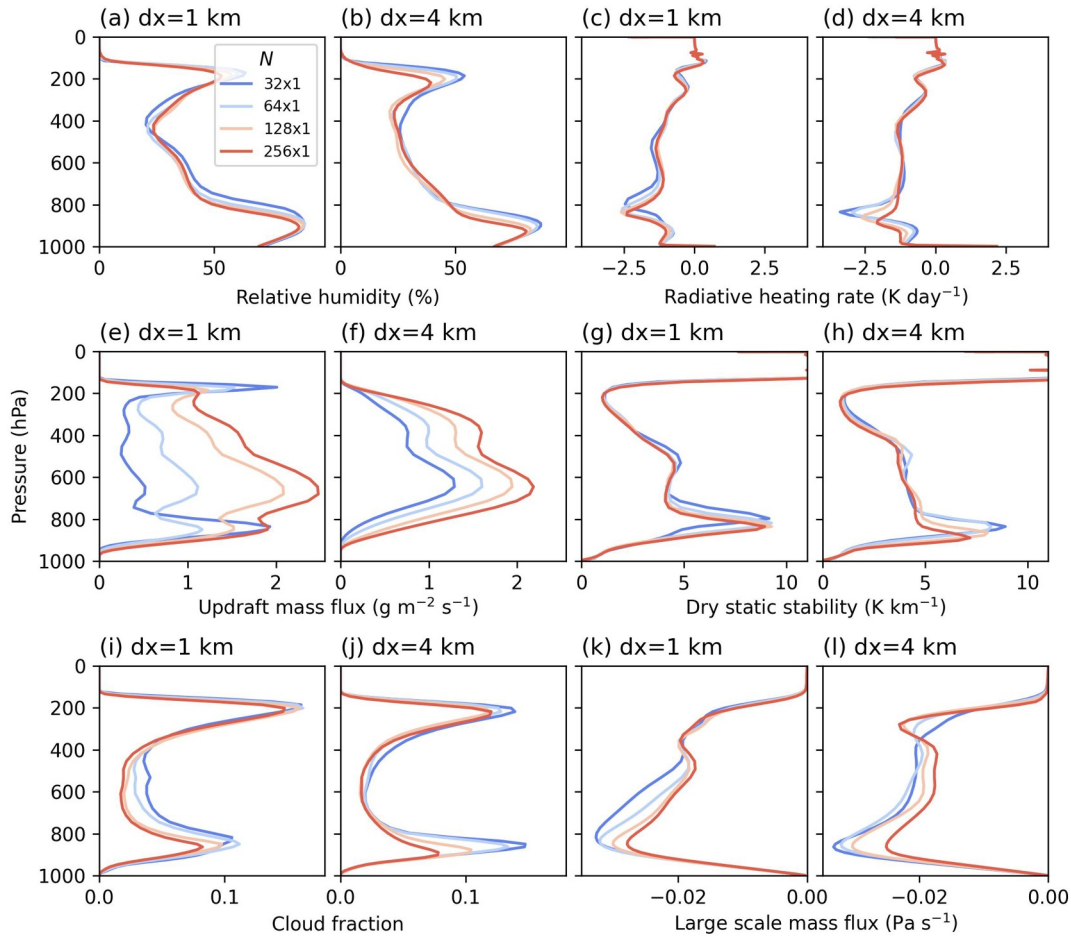

Figure 6. Domain mean profiles from E3SM-MMF simulations across days 110–200 (a), (b) relative humidity (c), (d) radiative heating rate (e), (f) updraft mass flux (g), (h) dry static stability (i), (j) cloud fraction, and (k, l) large-scale mass flux. The first and third (second and fourth) columns are for simulations with embedded CRM horizontal grid spacing of 1 km (4 km).

5. Summary

In simulations using convection resolving models (CRMs), small domains (i.e., domains with few grid columns) are used in both standalone simulations and within GCMs employing superparameterization or a multi-scale modeling framework.

Convective fractional area must be small in order to maintain positive buoyancy against a subsiding and warming environment. Small convective fractional area ensures that the downward mass flux is spread over a large area and hence, heats the environment slowly. This is the same argument used to explain the observed smallness of convective ascent area (Bjerknes, 1938). In CRM domains, the smallest possible convective fractional ascent area increases as the number of total grid columns, N decreases. Consequently, convective fractional ascent area is forced to be large in CRM domains with small N which causes a suppression of convection due to strong subsidence warming. This argument is presented qualitatively in Pritchard et al. (2014), and inspired Tompkins and Craig (1998) to conduct a scale analysis to find the minimum number of columns needed to support continuous convection ($N \approx 2400$).

Here, we present a heuristic analytic argument to show why convection is "throttled", or suppressed, for small N. We show that.

1. Domains with small N require more instability to sustain convection due to large convective fractional areas.
2. Updraft dilution by entrainment increases the critical instabiltiy needed to sustain convection.

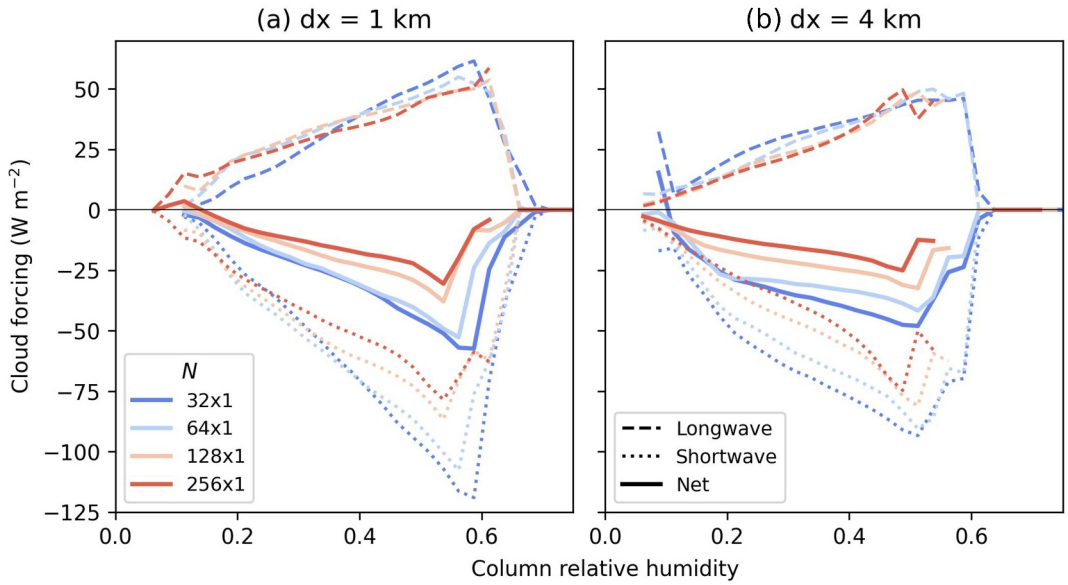

Figure 7. Cloud forcing (clear sky minus all sky top-of-atmosphere radiative flux) binned by column relative humidity (precipitable water divided by saturated precipitable water) for E3SM-MMF simulations with embedded CRM grid spacing of (a) 1 km and (b) 4 km. Dashed lines are the longwave cloud forcing, dotted lines are the shortwave cloud forcing, and the solid lines show the net (longwave plus shortwave) cloud forcing.

3. Enhanced updraft dilution occurs for small N, which may be due to restricted updraft size. This enhances the throttling effect of small N, and can be reduced by increasing the grid spacing to reduce updraft dilution.

We run standalone CRM simulations and GCM-coupled simulations in radiative-convective equilibrium to showcase these features in two frameworks: one where the CRM domain is in radiative-convective equilibrium (standalone CRM simulations), and one where the CRM domain may also horizontally exchange energy with other CRM domains via the GCM circulation.

In standalone CRM simulations with prescribed radiative heating tendencies, as a result of "throttled" convection, the domain mean instability increases for small N, and precipitation becomes more temporally variable, with periods of intense rain followed by relatively quiescent periods. Enhanced entrainment and detrainment in small domains increases the mean relative humidity, convective mass flux, and anvil cloud fraction. Increasing the grid spacing reduces the differences between N, consistent with reduced mixing and updraft dilution.

In GCM-coupled simulations, small N also leads to convective throttling. Smaller N simulations have more precipitable water, increased low-level relative humidity, and enhanced cloud radiative effects compared to larger N domains, consistent with Pritchard et al. (2014). However, spread in most fields is reduced compared to standalone simulations. Throttling in the presence of GCM-coupling causes the large-scale (i.e., GCM) circulation to be more intense for small N, and for the large-scale to exhibit more organization or clustering. Increasing grid spacing slightly reduces differences between simulations with varying N, with the largest differences in the mid-tropospheric cloud fraction.

6. Discussion

In this study, we discuss the modulation of convective throttling due to domain smallness (i.e., having few grid columns) by horizontal grid spacing. We emphasize that the heuristic model we present is not valid for large domains, especially those that support convective aggregation.

We pose that increasing grid spacing reduces convective throttling by allowing updrafts to be physically wider, and hence entrain less. While many studies have found a link between updraft width and entrainment rate (e.g., Hernandez-Deckers & Sherwood, 2018; Levine, 1959; McCarthy, 1974; Kirshbaum & Grant, 2012; Morrison, 2017; Morrison et al., 2020), the strength of this link is debated (e.g., Dawe & Austin, 2013; Xu et al., 2021), and may not be the pathway through which grid spacing affects updraft dilution (Jeevanjee & Zhou, 2022; Tang &

Kirshbaum, 2020). More work is needed to confirm the pathway through which grid spacing affects updraft buoyancy for simulations with small N. Additionally, because turbulent mixing is, in part, a sub-grid scale (and hence, parameterized) process, there may be some model variation.

We present results using simulations with a fixed sea surface temperature (SST), and did not explore any sea surface temperature dependence of convective throttling and how it is modulated by grid spacing. It is possible that changing the fixed SST impacts the dependence of simulated convection on CRM domain size. Both instability and the diluting effects of entrainment increase with SST (Singh & O'Gorman, 2015), which may either reduce or amplify throttling depending on which pathway is more enhanced via changes in SST. If SST indeed affects throttling, then climate change simulations using an SP/MMF-GCM may display nonphysical evolving convective statistics due to change in the strength of convective throttling. Since convective throttling has a clear impact on cloud radiative effects (Pritchard et al., 2014), and on convective organization, this deserves further study. Additionally, it remains unclear from our study how interactive SSTs may interact with convective throttling. This also deserves further study as feedbacks between SST, deep convection, and cloud shading are important for maintaining the observed near cancellation of shortwave and longwave cloud radiative effects in the tropical warm pool (Hartmann et al., 2001; Wall et al., 2019).

This study has direct implications for SP/MMF modeling, in which simulations using domains with few columns are still commonplace. While we note that throttling is reduced when grid spacing is coarsened, we do not necessarily advise using this fact as the sole basis upon which to choose coarse resolution in a SP/MMF setup. For example, coarse grid spacing may artificially enhance low-level cloudiness due to reduced mixing (Pauluis & Garner, 2006; Peng et al., 2024). Our simulations also show that moving from 1 to 4 km grid spacing is associated with a reduction in the mid-tropospheric cloud fraction and stability near the freezing level, which is an important part of the tropical convective cloud spectrum (Johnson et al., 1999). Reducing grid spacing is often seen as a desirable change as it permits explicit resolution of smaller eddies, which are important for climate-regulating marine stratocumulus clouds (Parishani et al., 2017; Peng et al., 2024). However, care must be taken when grid spacing is reduced as this may enhance the effects of "throttling" as mixing is enhanced.

This study also illustrates that the sensitivities observed in standalone CRM simulations may not directly translate to identical sensitivities when a CRM is coupled to a GCM in a SP/MMF setup.

The convective area fraction's tight control by the domain lapse rate is in part a result of domain mass conservation (Equation 1). We can write the condition for convection presented in Equation 4 because it is always true that environmental air is descending if there is convection occurring. Consider however the case where domain mass is not conserved, for example, in an SP/MMF-GCM where the CRM directly experiences the large-scale vertical motion of a host grid cell. Assuming condition (Equation 4) holds, (Equation 5) becomes

$$\sigma_c < \frac{\Gamma_c - \Gamma_m - \frac{\overline{w}}{w_c}}{\Gamma_d - \Gamma_m + \Gamma_c - \Gamma_e}, \tag{12}$$

where $\overline{w}$ is the mean circulation of the domain. If $\overline{w} < 0$, condition (Equation 4) is still valid. However, convection may be less "throttled" because the descending mean mass flux enables a larger maximum σ_c. That is, for a given computational domain size, convection may be triggered for less unstable profiles than is possible when $\overline{w}$ *must* be zero. For large-scale ascent ($\overline{w} > 0$), environmental air is no longer guaranteed to be sinking and warming, and we can not claim Equation 12 because of the potential for violation of the condition in Equation 4. Currently, in both E3SM-MMF and SP-CAM, any large-scale vertical motion occurring on the GCM grid is communicated to the embedded CRM via a horizontally uniform forcing on the temperature (and moisture) tendencies (Grabowski, 2001), rather than on the velocity field. This does not impact the limitation of convective fractional ascent by the local lapse rate written in Equation 5. It remains to be seen if convective throttling is reduced in super-parameterized simulations without strict enforcement of $\overline{w} = 0$.

Lastly, while quantitative, the argument we use to explain why a small CRM domain "throttles" convection relies on a minimalist depiction of relations between variables during convective motions. For example, radiation, which is not considered in our equations, may help reduce the critical lapse rate (Γ^*) needed to sustain an overturning circulation for a given computational domain size because it heats the convective region relative to the non-convective region and thus helps maintain the condition in Equation 4. Similarly, we do not consider

cooling in the environmental region due to evaporation of detrained condensate, which may further help to reduce Γ^*. It is possible that these processes may have stronger effects than we anticipate. While entrainment is considered in a mostly qualitative sense in our discussion of the limitation of updraft width by domain size, we show in Figure 1 that it can have a large impact on Γ^*. Nonetheless, we believe that the model captures the primary relationships between variables that help explain convective throttling in small domains.

Data Availability Statement

Convection resolving model simulations were conducted with the System for Atmospheric Modeling (SAM) version 6.10.6 (Khairoutdinov, 2022). The Energy Exascale Earth System Model (E3SM) project (E3SM Project, 2024) is sponsored by the U.S. Department of Energy, Office of Science, Office of Biological and Environmental Research Earth Systems Model Development Program area of Earth and Environmental System Modeling. The E3SM project, code, simulation configurations, model output, and tools to work with the output are described on its website (https://e3sm.org). Instructions on how to get started with running E3SM are available on the website (https://e3sm.org/model/running-e3sm/e3sm-quick-start). All code for E3SM may be accessed on the GitHub repository (https://github.com/E3SM-Project/E3SM). The raw output data from E3SM-MMF used in this study are archived in the National Energy Research Scientific Computing Center (NERSC). Simulation data to reproduce figures is archived and can be accessed from Zenodo (Jenney et al., 2025).

Acknowledgments

We thank the reviewers for their time and insightful comments, which improved the quality and utility of this manuscript. This research has been supported by the National Oceanic and Atmospheric Administration Climate and Global Change Postdoctoral Fellowship Program through UCAR CPAESS Grant NA18NWS4620043B. ZH acknowledges the funding from NSF Grant 1743753, from the Office of Biological and Environmental Research of the U.S. DOE under Grant DE-SC0022887 as part of the ASR Program, and the Grant DGE1745303 from NSF Graduate Research Fellowships Program. This work used Bridges-2 at Pittsburgh Supercomputing Center through allocation EES230034 from the Advanced Cyberinfrastructure Coordination Ecosystem: Services and Support (ACCESS, Boerner et al., 2023) program, which is supported by National Science Foundation grants 2138259, 2138286, 2138307, 2137603, and 2138296. Department of Energy Office of Science and the National Nuclear Security Administration and by the Energy Exascale Earth System Model (E3SM) project, funded by the U.S. Department of Energy, Office of Science, Office of Biological and Environmental Research. This work was performed under the auspices of the U.S. Department of Energy by Lawrence Livermore National Laboratory under Contract DE-AC52-07NA27344. This research used resources of the National Energy Research Scientific Computing Center (NERSC), a U.S. Department of Energy Office of Science User Facility operated under Contract No. DE-AC02-05CH11231. We thank Zhiming Kuang, Kerry Emanuel, Xueying Yu, Joey Smith, and Roger Samelson for helpful comments.

References

Beydoun, H., Caldwell, P. M., Hannah, W. M., & Donahue, A. S. (2021). Dissecting anvil cloud response to sea surface warming. *Geophysical Research Letters*, *48*(15). https://doi.org/10.1029/2021gl094049

Bjerknes, J. (1938). Saturated-adiabatic ascent of air through dry-adiabatically descending environment. *Quart. J. Roy. Meteor. Soc.*, *64*, 325–330.

Boerner, T. J., Deems, S., Furlani, T. R., Knuth, S. L., & Towns, J. (2023). ACCESS: Advancing innovation: NSF's advanced cyberinfrastructure coordination ecosystem: Services and support. In *Practice and experience in advanced research computing* (pp. 173–176). Association for Computing Machinery.

Dawe, J. T., & Austin, P. H. (2013). Direct entrainment and detrainment rate distributions of individual shallow cumulus clouds in an LES. *Atmospheric Chemistry and Physics*, *13*(15), 7795–7811. https://doi.org/10.5194/acp-13-7795-2013

De Rooy, W. C., Bechtold, P., Fröhlich, K., Hohenegger, C., Jonker, H., Mironov, D., et al. (2013). Entrainment and detrainment in cumulus convection: An overview. *Quarterly Journal of the Royal Meteorological Society*, *139*(670), 1–19. https://doi.org/10.1002/qj.1959

E3SM Project. (2024). *Energy Exascale Earth System Model (E3SM)*. [Computer Software]. https://doi.org/10.11578/E3SM/dc.20240301.3

Golaz, J., Caldwell, P. M., Van Roekel, L. P., Petersen, M. R., Tang, Q., Wolfe, J. D., et al. (2019). The DOE E3SM coupled model version 1: Overview and evaluation at standard resolution. *Journal of Advances in Modeling Earth Systems*, *11*(7), 2018MS001603. https://doi.org/10.1029/2018MS001603

Grabowski, W. W. (2001). Coupling cloud processes with the Large-Scale dynamics using the Cloud-Resolving convection parameterization (CRCP). *Journal of the Atmospheric Sciences*, *58*(9), 978–997. https://doi.org/10.1175/1520-0469(2001)058<0978:ccpwtl>2.0.co;2

Grabowski, W. W., & Smolarkiewicz, P. K. (1999). CRCP: A cloud resolving convection parameterization for modeling the tropical convecting atmosphere. *Physica D*, *133*(1), 171–178. https://doi.org/10.1016/s0167-2789(99)00104-9

Hannah, W. M. (2017). Entrainment versus dilution in tropical deep convection. *Journal of the Atmospheric Sciences*, *74*(11), 3725–3747. https://doi.org/10.1175/JAS-D-16-0169.1

Hannah, W. M., Bradley, A. M., Guba, O., Tang, Q., Golaz, J.-C., & Wolfe, J. (2021). Separating physics and dynamics grids for improved computational efficiency in spectral element Earth System models. *Journal of Advances in Modeling Earth Systems*, *13*(7), e2020MS002419. https://doi.org/10.1029/2020MS002419

Hannah, W. M., Jones, C. R., Hillman, B. R., Norman, M. R., Bader, D. C., Taylor, M. A., et al. (2020). Initial results from the super-parameterized E3SM. *Journal of Advances in Modeling Earth Systems*, *12*(1). https://doi.org/10.1029/2019ms001863

Hannah, W. M., & Pressel, K. (2022). A method for transporting cloud-resolving model variance in a multiscale modeling framework. *Geoscientific Model Development*, *15*(24), 8999–9013. https://doi.org/10.5194/gmd-15-8999-2022

Hannah, W. M., Pressel, K., Ovchinnikov, M., & Elsaesser, G. (2022). Checkerboard patterns in e3smv2 and e3sm-mmfv2. *Geoscientific Model Development*, *15*(15), 6243–6257. https://doi.org/10.5194/gmd-15-6243-2022

Hartmann, D. L., Moy, L. A., & Fu, Q. (2001). Tropical convection and the energy balance at the top of the atmosphere. *Journal of Climate*, *14*(24), 4495–4511. https://doi.org/10.1175/1520-0442(2001)014<4495:tcateb>2.0.co;2

Hernandez-Deckers, D., & Sherwood, S. C. (2018). On the role of entrainment in the fate of cumulus thermals. *Journal of the Atmospheric Sciences*, *75*(11), 3911–3924. https://doi.org/10.1175/jas-d-18-0077.1

Holtslag, A. A. M., & Boville, B. A. (1993). Local versus nonlocal boundary-layer diffusion in a global climate model. *Journal of Climate*, *6*(10), 1825–1842. https://doi.org/10.1175/1520-0442(1993)006(1825:LVNBLD)2.0.CO;2

Hsu, W.-C., Kooperman, G. J., & Hannah, W. M. (2024). Investigating mechanisms driving differences in the characteristics of precipitation in 3 the E3SM multiscale modeling framework with 2D vs 3D cloud resolving model configurations. *Journal of Advances in Modeling Earth Systems*, *17*(1). https://doi.org/10.1029/2024ms004274

Iacono, M. J., Delamere, J. S., Mlawer, E. J., Shephard, M. W., Clough, S. A., & Collins, W. D. (2008). Radiative forcing by long-lived greenhouse gases: Calculations with the AER radiative transfer models. *Journal of Geophysical Research*, *113*(D13). https://doi.org/10.1029/2008jd009944

Jansson, F., van den Oord, G., Pelupessy, I., Chertova, M., Grönqvist, J. H., Siebesma, A. P., & Crommelin, D. (2022). Representing cloud mesoscale variability in superparameterized climate models. *Journal of Advances in Modeling Earth Systems*, *14*(8). https://doi.org/10.1029/2021ms002892

Jansson, F., van den Oord, G., Pelupessy, I., Grönqvist, J. H., Siebesma, A. P., & Crommelin, D. (2019). Regional superparameterization in a global circulation model using large eddy simulations. *Journal of Advances in Modeling Earth Systems*, *11*(9), 2958–2979. https://doi.org/10.1029/2018ms001600

Jeevanjee, N., & Zhou, L. (2022). On the resolution-dependence of anvil cloud fraction and precipitation efficiency in radiative-convective equilibrium. *Journal of Advances in Modeling Earth Systems*, *14*(3). https://doi.org/10.1029/2021ms002759

Jenney, A., Hu, Z., & Hannah, W. (2025). On the dependence of simulated convection on domain size in crms: Data for figures. *Zenodo*. [Data]. https://doi.org/10.5281/zenodo.14675104

Johnson, R. H., Rickenbach, T. M., Rutledge, S. A., Ciesielski, P. E., & Schubert, W. H. (1999). Trimodal characteristics of tropical convection. *Journal of Climate*, *12*(8), 2397–2418. https://doi.org/10.1175/1520-0442(1999)012<2397:tcotc>2.0.co;2

Khairoutdinov, M. F. (2022). System for atmospheric modeling (version 6.10.6). [Software] http://rossby.msrc.sunysb.edu/~marat/SAM/

Khairoutdinov, M. F., DeMott, C., & Randall, D. (2008). Evaluation of the simulated interannual and subseasonal variability in an AMIP-style simulation using the CSU multiscale modeling framework. *Journal of Climate*, *21*(3), 413–431. https://doi.org/10.1175/2007jcli1630.1

Khairoutdinov, M. F., & Randall, D. (2006). High-Resolution simulation of Shallow-to-Deep convection transition over land. *Journal of the Atmospheric Sciences*, *63*(12), 3421–3436. https://doi.org/10.1175/jas3810.1

Khairoutdinov, M. F., Randall, D., & DeMott, C. (2005). Simulations of the atmospheric general circulation using a Cloud-Resolving model as a superparameterization of physical processes. *Journal of the Atmospheric Sciences*, *62*(7), 2136–2154. https://doi.org/10.1175/jas3453.1

Khairoutdinov, M. F., & Randall, D. A. (2003). Cloud resolving modeling of the ARM summer 1997 IOP: Model formulation, results, uncertainties, and sensitivities. *Journal of the Atmospheric Sciences*, *60*(4), 607–625. https://doi.org/10.1175/1520-0469(2003)060<0607:crmota>2.0.co;2

Kirshbaum, D. J., & Grant, A. L. M. (2012). Invigoration of cumulus cloud fields by mesoscale ascent. *Quart. J. Roy. Meteor. Soc.*, *138*(669), 2136–2150. https://doi.org/10.1002/qj.1954

Kogan, Y. L. (2021). LES study of precipitation/condensation dependance on cumulus clouds dynamics. *Advances in Science and Research*, *18*, 89–92. https://doi.org/10.5194/asr-18-89-2021

Kogan, Y. L. (2022). Condensation–mass flux connection in warm convective clouds: Theory and implications for cloud supersaturation. *Advances in Science and Research*, *19*, 91–95. https://doi.org/10.5194/asr-19-91-2022

Kuang, Z., & Bretherton, C. S. (2006). A mass-flux scheme view of a high-resolution simulation of a transition from shallow to deep cumulus convection. *Journal of the Atmospheric Sciences*, *63*(7), 1895–1909. https://doi.org/10.1175/jas3723.1

Levine, J. (1959). Spherical vortex theory of bubble-like motion in cumulus clouds. *Journal of Meteorology*, *16*(6), 653–662. https://doi.org/10.1175/1520-0469(1959)016<0653:svtobl>2.0.co;2

Lin, G., Jones, C. R., Leung, L. R., Feng, Z., & Ovchinnikov, M. (2022). Mesoscale convective systems in a superparameterized E3SM simulation at high resolution. *Journal of Advances in Modeling Earth Systems*, *14*(1). https://doi.org/10.1029/2021ms002660

Liu, N., Pritchard, M. S., Jenney, A. M., & Hannah, W. M. (2023). Understanding precipitation bias sensitivities in E3SM-multi-scale modeling framework from a dilution framework. *Journal of Advances in Modeling Earth Systems*, *15*(4). https://doi.org/10.1029/2022ms003460

McCarthy, J. (1974). Field verification of the relationship between entrainment rate and cumulus cloud diameter. *Journal of the Atmospheric Sciences*, *31*(4), 1028–1039. https://doi.org/10.1175/1520-0469(1974)031<1028:fvotrb>2.0.co;2

Morrison, H. (2017). An analytic description of the structure and evolution of growing deep cumulus updrafts. *Journal of the Atmospheric Sciences*, *74*(3), 809–834. https://doi.org/10.1175/jas-d-16-0234.1

Morrison, H., Peters, J. M., Varble, A. C., Hannah, W. M., & Giangrande, S. E. (2020). Thermal chains and entrainment in cumulus updrafts. part i: Theoretical description. *Journal of the Atmospheric Sciences*, *77*(11), 3637–3660. https://doi.org/10.1175/jas-d-19-0243.1

Muller, C. J., & Held, I. M. (2012). Detailed investigation of the Self-Aggregation of convection in Cloud-Resolving simulations. *Journal of the Atmospheric Sciences*, *69*(8), 2551–2565. https://doi.org/10.1175/jas-d-11-0257.1

Norman, M., Lyngaas, I., Bagusetty, A., & Berrill, M. (2023). Portable c++ code that can look and feel like FORTRAN code with yet another kernel launcher (YAKL). *International Journal of Parallel Programming*, *51*(4–5), 209–230. https://doi.org/10.1007/s10766-022-00739-0

Parishani, H., Pritchard, M. S., Bretherton, C. S., Wyant, M. C., & Khairoutdinov, M. F. (2017). Toward low-cloud-permitting cloud superparameterization with explicit boundary layer turbulence: LOW-CLOUD ultraparameterization. *Journal of Advances in Modeling Earth Systems*, *9*(3), 1542–1571. https://doi.org/10.1002/2017ms000968

Pauluis, O., & Garner, S. (2006). Sensitivity of Radiative–Convective equilibrium simulations to horizontal resolution. *Journal of the Atmospheric Sciences*, *63*(7), 1910–1923. https://doi.org/10.1175/jas3705.1

Peng, L., Blossey, P. N., Hannah, W. M., Bretherton, C. S., Terai, C. R., Jenney, A. M., & Pritchard, M. (2024). Improving stratocumulus cloud amounts in a 200-m resolution multi-scale modeling framework through tuning of its interior physics. *Journal of Advances in Modeling Earth Systems*, *16*(3), e2023MS003632. https://doi.org/10.1029/2023ms003632

Pritchard, M. S., Bretherton, C. S., & DeMott, C. A. (2014). Restricting 32-128 km horizontal scales hardly affects the MJO in the superparameterized community atmosphere model v.3.0 but the number of cloud-resolving grid columns constrains vertical mixing. *Journal of Advances in Modeling Earth Systems*, *6*(3), 723–739. https://doi.org/10.1002/2014ms000340

Randall, D., Khairoutdinov, M. F., Arakawa, A., & Grabowski, W. (2003). Breaking the cloud parameterization deadlock. *Bulletin America Meteorology Social*, *84*(11), 1547–1564. https://doi.org/10.1175/bams-84-11-1547

Romps, D. M. (2012). Weak pressure gradient approximation and its analytical solutions. *Journal of the Atmospheric Sciences*, *69*(9), 2835–2845. https://doi.org/10.1175/jas-d-11-0336.1

Rousseau-Rizzi, R., Kirshbaum, D. J., & Yau, M. K. (2017). Initiation of deep convection over an idealized mesoscale convergence line. *Journal of the Atmospheric Sciences*, *74*(3), 835–853. https://doi.org/10.1175/jas-d-16-0221.1

Seeley, J. T., Jeevanjee, N., Langhans, W., & Romps, D. M. (2019). Formation of tropical anvil clouds by slow evaporation. *Geophysical Research Letters*, *46*(1), 492–501. https://doi.org/10.1029/2018gl080747

Singh, M. S., & O'Gorman, P. A. (2015). Increases in moist-convective updraught velocities with warming in radiative-convective equilibrium. *Quart. J. Roy. Meteor. Soc.*, *141*(692), 2828–2838. https://doi.org/10.1002/qj.2567

Tang, S. L., & Kirshbaum, D. J. (2020). On the sensitivity of deep-convection initiation to horizontal grid resolution. *Quarterly Journal of the Royal Meteorological Society*, *146*(728), 1085–1105. https://doi.org/10.1002/qj.3726

Tompkins, A. M., & Craig, G. C. (1998). Radiative–convective equilibrium in a three-dimensional cloud-ensemble model. *Quart. J. Roy. Meteor. Soc.*, *124*(550), 2073–2097. https://doi.org/10.1256/smsqj.55012

Wall, C. J., Hartmann, D. L., & Norris, J. R. (2019). Is the net cloud radiative effect constrained to be uniform over the tropical warm pools? *Geophysical Research Letters*, *46*(21), 12495–12503. https://doi.org/10.1029/2019gl083642

Wing, A. A., Emanuel, K., Holloway, C. E., & Muller, C. (2017). Convective self-aggregation in numerical simulations: A review. *Surveys in Geophysics*, *38*(6), 1173–1197. https://doi.org/10.1007/s10712-017-9408-4

Wing, A. A., Reed, K. A., Satoh, M., Stevens, B., Bony, S., & Ohno, T. (2018). Radiative–convective equilibrium model intercomparison project. *Geoscientific Model Development*, *11*(2), 793–813. https://doi.org/10.5194/gmd-11-793-2018

Xu, X., Sun, C., Lu, C., Liu, Y., Zhang, G. J., & Chen, Q. (2021). Factors affecting entrainment rate in deep convective clouds and parameterizations. *JGR Atmospheres*, *126*(15). https://doi.org/10.1029/2021jd034881

Yanase, T., Nishizawa, S., Miura, H., Takemi, T., & Tomita, H. (2020). New critical length for the onset of self-aggregation of moist convection. *Geophysical Research Letters*, *47*(16). https://doi.org/10.1029/2020gl088763

Yano, J.-I. (2014). Formulation structure of the mass-flux convection parameterization. *Dynamics of Atmospheres and Oceans*, *67*, 1–28. https://doi.org/10.1016/j.dynatmoce.2014.04.002